Electrodeposition of bismuth from nitric acid electrolyte

E. Sandnes, M.E. Williams, U. Bertocci [1], M.D. Vaudin, G.R. Stafford [*]

Materials Science and Engineering Laboratory, National Institute of Standards and Technology, Gaithersburg, Maryland 20899, USA

Abstract

The electrodeposition of Bi from acidic nitrate solution was examined. Bismuth deposition was determined to be quasi-reversible on Au, with a current efficiency of 100%, based on integration of deposition and stripping voltammetric waves. No interference from nitrate reduction was found on Bi and Au, whereas nitrate reduction occurred on W and Cu electrodes. Analysis of current-time transients clearly shows nucleation on Au to be instantaneous. Field emission SEM revealed nodular deposits with moderate surface roughness. Nodule size varied from 1 to 5 μm depending on deposition potential and deposit thickness. X-ray diffraction (XRD) patterns for all deposits were indexed to rhombohedral bismuth. The deposits showed fairly strong (0 1 2) crystallographic texture at high deposition overpotentials.
© 2007 Elsevier Ltd. All rights reserved.

Keywords: Electrodeposition; Bismuth; Nucleation; Texture; Thin film

1. Introduction

In recent years, bismuth deposition has become an interesting subject for the electrochemical community because of bismuth's unique electrical, physical and chemical properties. Bismuth thin films have shown large magnetoresistance [1–3], thermoelectric efficiency [4] and interesting quantum effects [5]. Bismuth is also used in electrochromic devices, [6,7] and for contact formation on semiconductors [8]. Highly textured Bi films have been electrodeposited onto semiconductor substrates [9–11]. Uses of thin bismuth film electrodes in electrochemical stripping analysis offer a very attractive alternative to mercury electrodes due to the much more environmentally friendly bismuth [12–14]. Sub-monolayers of bismuth on some noble metal surfaces have shown enhanced catalytic activity for a variety of electrochemical processes, most notably the two-electron reduction of H_2O_2 to H_2O, often the limiting step in the reduction of O_2 in aqueous fuel cells [15,16], as well as the oxidation of formic acid on Pt [17–21].

Much of the bismuth deposition literature has focused either on its underpotential deposition (upd) onto noble metals or its nucleation and growth onto non-metallic substrates, such as glassy carbon [22] and semiconductors [9–11]. There is a paucity of bismuth electrodeposition literature involving the growth of continuous films onto metallic substrates [23,24]. In this paper, we examine the electrodeposition of bismuth films, up to 15 μm thick, from nitric acid electrolyte. The electrochemical reduction of Bi^{3+} on Au was explored using cyclic voltammetry (CV), chronoamperometry, and an electrochemical quartz crystal nanobalance (EQNB). The surface morphology and crystal structure of bismuth, electrodeposited onto both gold and copper substrates, were characterized by X-ray diffraction (XRD) and with a field emission scanning electron microscope (FE-SEM) equipped with a focused ion beam (FIB).

2. Experimental

The electrodeposition of bismuth was examined in 1.0 mol L^{-1} HNO$_3$ containing controlled additions of Bi(NO$_3$)$_3$. The solutions were made from 99.999% Bi(NO$_3$)$_3$·H$_2$O (Sigma–Aldrich, Inc., USA[2]) and nitric acid, 69.4% (J.T. Baker, USA). In order to dissolve the Bi(NO$_3$)$_3$·H$_2$O, an acidic solution was required. Distilled water was further purified (to 18.3 MΩ cm) using an EASY pure UV ultrapure water system (Barnstead). All electrolytes were purged with nitrogen prior to

---

* Corresponding author. Tel.: +1 301 975 6412; fax: +1 301 926 7679.
E-mail address: gery.stafford@nist.gov (G.R. Stafford).
[1] ISE member.

and during experiments. The electrochemical experiments were carried out using a potentiostat/galvanostat (model 173) together with a universal programmer (model 175) both from Princeton Applied Research, EG&G Company. Data were digitized from the analog output by means of a MacAdios II data acquisition board in a MacIntosh IIcx personal computer.

The electrochemical measurements were performed at room temperature, in a single-compartment cell covered with a polyethylene film to prevent air entering the compartment. A platinum counter electrode was positioned in the same compartment as the working electrode. A saturated Hg sulfate electrode (SSE) was used as a reference electrode. All potentials are given with respect to this reference. A Vycor-tipped bridge filled with $0.1\,mol\,L^{-1}$ H_2SO_4 separated the SSE from the working compartment.

A variety of electrode materials was used in the voltammetric examination. These included a polycrystalline gold rod measuring 4.5 mm in diameter and 1.6 cm in length, a 250 nm thick Au film which had been vapor-deposited onto a borosilicate glass substrate, a copper wire measuring 0.8 mm in diameter and 2.0 cm in length, a cross-section of a 1.0 mm diameter gold wire sealed in epoxy, and a cross-section of a 0.8 mm diameter tungsten wire sealed in glass. The gold wire and the tungsten wire cross-sections were wet-polished with #2400 and #4000 SiC-paper. All electrodes were rinsed thoroughly with acetone, ethanol and distilled water prior to use. The Au electrodes were further cleaned by continuously sweeping the potential for 30 min prior to the voltammetric measurements.

Gold and copper electrodes were used for preparation of the Bi deposits for microscopic and X-ray examination. The gold electrode consisted of a 250 nm thick gold film which had been vapor-deposited onto a borosilicate glass substrate which had first been coated with a Ti bonding layer. The film had a strong (1 1 1) crystallographic orientation. The copper substrates were polycrystalline sheets, wet-polished in the same manner as the cross-sectioned electrodes. All deposits were made in $1.0\,mol\,L^{-1}$ HNO_3 containing $0.10\,mol\,L^{-1}$ $Bi(NO_3)_3$. Deposition was terminated when the charge reached the value corresponding to the desired thickness. The deposits were immediately removed from the cell, rinsed in distilled water and blown dry with air. The electrodeposits were examined by X-ray diffraction, using a Siemens D-500 diffractometer and Cu Kα radiation, and by field emission SEM using a Hitachi S4700 operating at 5 kV and 30 μA. Bismuth cross-sections were prepared using a dual beam FIB (FEI Company) model DB620 operating at 30 kV and milling currents down to 350 pA.

Mass changes during Bi deposition were monitored by means of an electrochemical quartz nanobalance (EQNB). The instrument was a RQCM (Maxtek, Inc.). The quartz crystals used were polished 2.54 cm AT cut blanks (Maxtek, Inc.), onto which first Ti and then Au was evaporated. Their resonance frequency was 5 MHz. The EQNB as well as the EG&G 273 potentiostat/galvanostat were run by Labview™ software on a Macintosh Power PC computer. The cell, in which the Au-covered quartz crystal was the working electrode, had a separated compartment for the Pt counter electrode and a SSE reference electrode connected via a Luggin-Haber capillary. The

cell had a magnetic stirrer, and N_2 could be bubbled into the main compartment to deaerate the solution, or could flow above the solution, maintaining a small positive pressure inside the cell. The measurements were carried out in galvanostatic mode.

3. Results and discussion

Initial experiments on tungsten in $1.0\,mol\,L^{-1}$ HNO_3 revealed a large nitrate reduction peak at a potential positive to hydrogen evolution. The reduction started at a potential of $-0.70\,V$ versus SSE. Several reactions are suggested for nitrate reduction in the literature [25]. The only reaction occurring in the same potential range as that observed experimentally is the reaction:

$$NO_3^- + H_2O + 2e^- = NO_2^- + 2OH^- \tag{1}$$
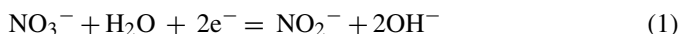
which is reported to have a standard potential of 0.010 V versus the standard hydrogen electrode (SHE) which corresponds to $-0.630\,V$ versus the SSE [25]. In electrolytes containing Bi^{3+}, any occurrence of nitrate reduction in the potential range where Bi^{3+} reduction or hydrogen evolution occur would complicate the interpretation of the voltammograms due to the unknown current contribution from Reaction (1). As a consequence, information about the ability of bismuth, gold and copper to reduce nitrate or evolve hydrogen then becomes significant. Fig. 1 presents voltammograms for Bi, Au, Cu and W electrodes in $1.0\,mol\,L^{-1}$ HNO_3. Tungsten and Cu both show a catalytic activity for nitrate reduction. In the case of W, reduction starts at $-0.70\,V$, and a current peak is observed at a potential of $-0.83\,V$. At about $-1.0\,V$ hydrogen evolution begins on the tungsten surface. Nitrate reduction on Cu occurs positive of the H_2 reversible potential and about 0.1 V anodic of that observed for W. In the case of Bi, hydrogen evolution was the only reaction observed, starting at a potential of about $-0.90\,V$. The Au electrode showed a reduction current starting at $-0.65\,V$, which is about 10 mV negative of the reversible hydrogen potential. Additional voltammograms for a Pt electrode (not shown in Fig. 1) showed a reduction current starting at the same potential. Con-
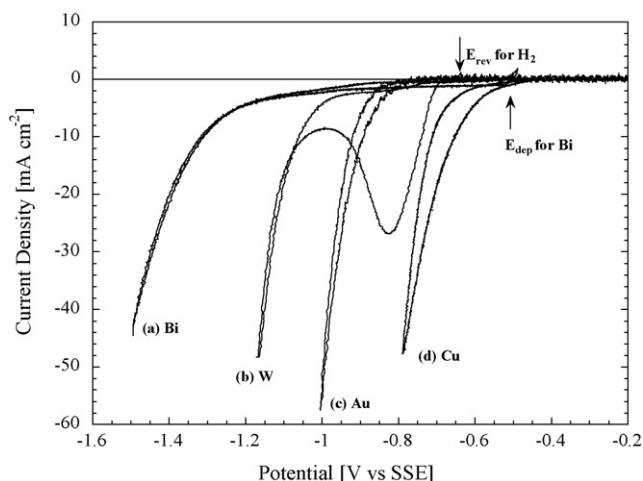

Fig. 1. Voltammograms for (a) Bi, (b) W, (c) Au, and (d) Cu electrodes in $1.0\,mol\,L^{-1}$ HNO_3. Sweep rate is $100\,mV\,s^{-1}$.
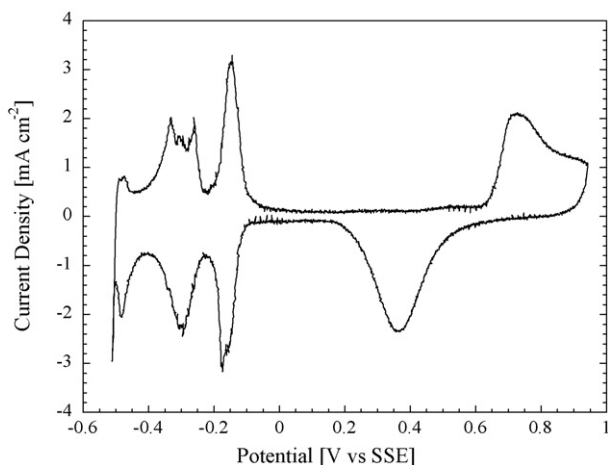
Fig. 2. Cyclic voltammogram ($1.0\,V\,s^{-1}$) of evaporated (1 1 1)-textured Au in $1.0\,mol\,L^{-1}$ HNO$_3$ containing $0.020\,mol\,L^{-1}$ Bi(NO$_3$)$_3$. Bulk deposition of Bi starts at $-0.500\,V$ vs. SSE.

Fig. 3. Cyclic voltammograms on Au wire electrode in $1.0\,mol\,L^{-1}$ HNO$_3$ containing $0.020\,mol\,L^{-1}$ Bi(NO$_3$)$_3$ at sweep rates of (a) $0.5\,V\,s^{-1}$, (b) $2.0\,V\,s^{-1}$, (c) $5.0\,V\,s^{-1}$, and (d) $10.0\,V\,s^{-1}$.

sidering the high catalytic activity for hydrogen reduction on Au and Pt, the observed reduction current on Au is probably due to hydrogen evolution. These observations support reports in the literature where Au voltammetry in a solution of $0.5\,mol\,L^{-1}$ H$_2$SO$_4$ + $0.1\,mol\,L^{-1}$ NaNO$_3$ showed that the electroreduction of nitrate is very slow and marginally detectable [26]. The activity for nitrate electroreduction was reported to decrease in the order: Cu > Ag > Au. We conclude that Au electrodes are suitable for examining the reduction of Bi^{3+} in acidic nitrate solutions.

Fig. 2 shows the Bi^{3+} voltammetry on (1 1 1)-textured evaporated Au in $1.0\,mol\,L^{-1}$ HNO$_3$ containing $20\,mmol\,L^{-1}$ Bi^{3+} in the Bi upd region. Bismuth upd occurs in three steps that commence at about $-0.10\,V$, about $0.3\,V$ negative of the Au oxide region. The location of these voltammetric peaks is very similar to that reported by others in HNO$_3$ [27,28]. Bismuth forms two surface structures on Au (1 1 1) in the upd region. At low coverage, Bi forms a (2×2) structure, commensurate with the underlying Au surface [16,23,29–31]. At higher coverage, the (2×2) structure is replaced by a uniaxially commensurate ($p \times \sqrt{3}$)-2Bi adlayer [16,23,29–31]. Bismuth upd is an important step in the bulk deposition of Bi onto Au since nucleation and growth proceeds on the ($p \times \sqrt{3}$)-2Bi adlayer.

Fig. 3 shows the voltammetry for Bi deposition onto a cross-sectioned Au wire electrode in $1.0\,mol\,L^{-1}$ HNO$_3$ containing $0.020\,mol\,L^{-1}$ Bi(NO$_3$)$_3$ as a function of sweep rate. The voltammetry is consistent with that typically observed in metal deposition–stripping processes, although the overpotential associated with Bi nuclei formation on Au is not particularly significant. This is likely due to the presence of the Bi upd layer. No co-evolution of hydrogen occurs since the Bi reduction wave is completed prior to the potential where H$_2$ evolution begins on either Au or Bi. Thus, the peak current for bismuth reduction has no contribution from other electrochemical reactions. In addition, we observe a negative shift in the cathodic peak potential with sweep rate. Such a shift is typically associated with quasi-reversible electrochemical reactions. For a reversible process with an insoluble product, a theoretical treatment of the diffusion equations and boundary conditions yields a linear cor-
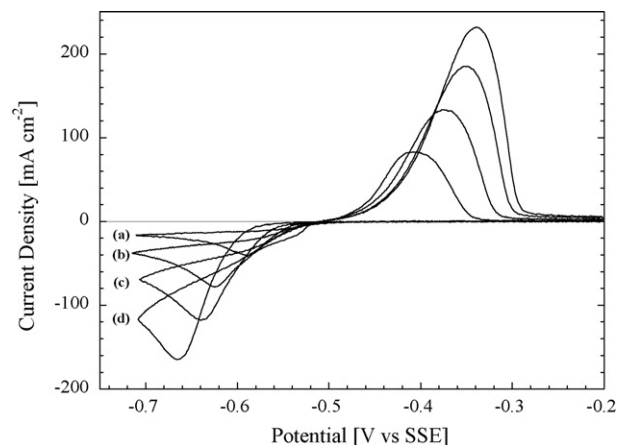
relation between the peak current versus the square root of the sweep rate, [32]:

$$i_p = 367n^{3/2}AC_0D^{1/2}\upsilon^{1/2} \tag{2}$$

where the variables and units are: i_p (current at peak [A]), n (equivalents mol^{-1}), A (electrode area [cm^2]), C_0 (bulk electroactive concentration [mol L^{-1}]), D (diffusion coefficient [cm^2 s^{-1}]), and υ (sweep rate [V s^{-1}]). Fig. 4 shows a plot of the peak current density versus the square root of the sweep rate for the voltammograms presented in Fig. 3. For $0.020\,mol\,L^{-1}$ Bi(NO$_3$)$_3$ in $1.0\,mol\,L^{-1}$ HNO$_3$ a linear relation is observed for sweep rates in the range of $0.010–10.0\,V\,s^{-1}$. An extrapolated linear regression of the data crosses the current axis near the origin, indicating a diffusion controlled process. Based on the slope of the linear regression, a Bi^{3+} diffusion coefficient was found to be $1.72 \times 10^{-6}\,cm^2\,s^{-1}$. This is reasonably close to the $2.75 \times 10^{-6}\,cm^2\,s^{-1}$ value we calculated from similar voltammetric data reported by Vereecken and Searson [11] using n^+-GaAs electrodes in nitrate-based electrolyte. In an electrolyte containing $0.10\,mol\,L^{-1}$ Bi(NO$_3$)$_3$ we have
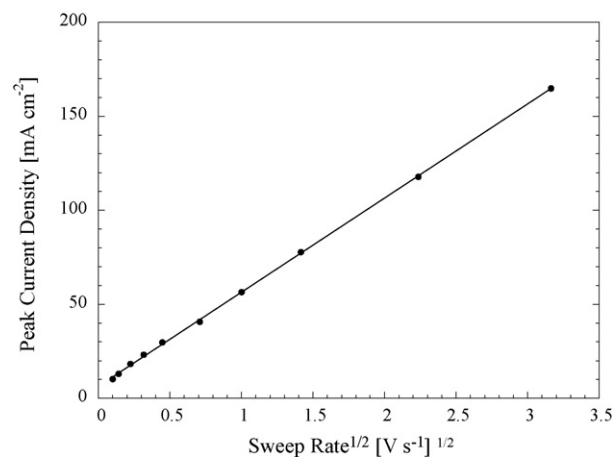

Fig. 4. Plot of the peak current vs. the square root of the sweep rate for the voltammograms presented in Fig. 3. The slope of the linear regression line is $50.0\,mA\,V^{1/2}\,s^{-1/2}\,cm^{-2}$.

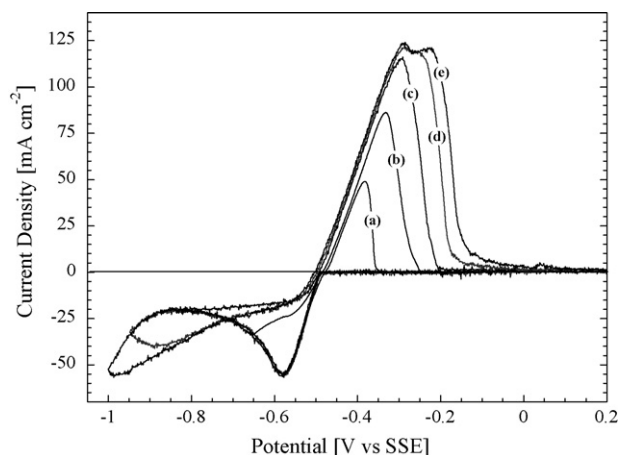Fig. 5. Cyclic voltammograms on polycrystalline Au cylinder in $1.0 \, \text{mol} \, \text{L}^{-1}$ HNO_3 containing $0.10 \, \text{mol} \, \text{L}^{-1}$ $Bi(NO_3)_3$. The cathodic vertex was varied to (a) -0.55 V, (b) -0.65 V, (c) -0.85 V, (d) -0.95 V, and (e) -1.0 V at constant sweep rate of $50 \, \text{mV} \, \text{s}^{-1}$.

Fig. 6. Current transients for Bi deposition onto a Au wire electrode in $1.0 \, \text{mol} \, \text{L}^{-1}$ HNO_3 containing $0.020 \, \text{mol} \, \text{L}^{-1}$ $Bi(NO_3)_3$ for different deposition potentials. The starting potential was -0.40 V. Inset plot shows i vs. $t^{-1/2}$.

observed a plot similar to that in Fig. 4 except for a slight deviation from linearity at higher sweep rates due to IR drop as a result of the higher deposition currents.

The current efficiency for the Fig. 3 voltammetry was calculated by integrating the current associated with the deposition and dissolution reactions. In $0.020 \, \text{mol} \, \text{L}^{-1}$ Bi^{3+} the current efficiency was independent of sweep rate in the range of 0.050–$10.0 \, \text{V} \, \text{s}^{-1}$. The average current efficiency was $101\% \pm 1\%$. Changing the lower vertex down to -0.90 V at a constant sweep rate of $0.050 \, \text{V} \, \text{s}^{-1}$, did not affect the current efficiency, which was $101\% \pm 2\%$. The voltammograms for the latter set of experiments are shown in Fig. 5. Decreasing the cathodic vertex beyond -0.90 V resulted in a rapid loss of current efficiency as loosely attached dendrites formed and detached from the electrode. The increase of the cathodic current in this same potential window reflects the morphological instability as the dendrites escape the diffusion layer and benefit from spherical diffusion. The formation of dendrites at the most negative potentials also altered the shape of the anodic dissolution peaks.

Nucleation transients from potential step measurements are shown in Fig. 6. Prior to initiating the potential step, the electrode was pre-conditioned at a potential of -0.40 V. Since this potential is in the Bi upd region (see Fig. 2) a sub-monolayer of Bi is present on the Au surface prior to deposition. After applying the potential step, the initial current increase arises from the charging of the double layer. Within the first 25 ms, a very small current peak is observed which we attribute to the completion of the Bi upd monolayer. This is followed by a larger potential-dependent current maximum which is typically attributed to nucleation and growth. In this latter region, the current maximum (i_{max}) increases while the time (t_{max}) required to reach i_{max} decreases with increasing overpotential as a consequence of the higher nucleation densities. At deposition potentials more negative than -0.53 V, the maximum in the nucleation current becomes less defined due to relatively higher currents from double layer charging. The final feature in the current transients is a Cottrell-type ($t^{-1/2}$) relaxation as individual spherical diffu-
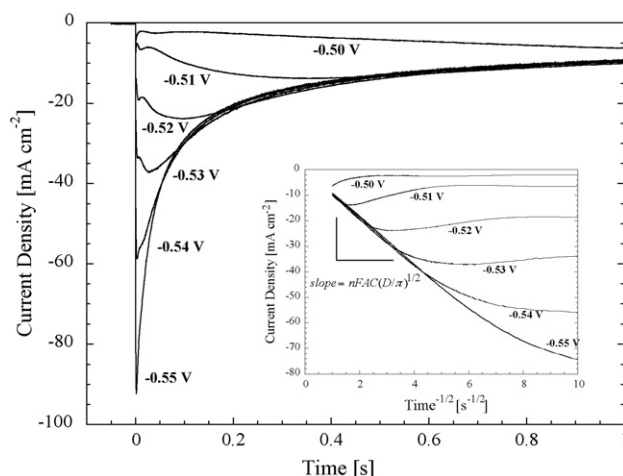
sion zones overlap to form a linear diffusion gradient [33]. At deposition potentials more negative than -0.51 V, the Cottrell currents are identical, indicating that deposition is diffusion-limited. Plots of i versus $t^{-1/2}$ yield straight lines of equal slope that intersect the origin. This is shown in the inset plot of Fig. 6.

Transients containing two current maxima in the nucleation region, like those shown in Fig. 6, are often observed in Stranski-Krastanov growth where one or more monolayers grow two-dimensionally prior to three-dimensional island growth [34–36]. Palomar-Pardave et al. have developed a quantitative treatment by simulating the various contributions to the nucleation and growth process [36,37], specifically double layer charging, two-dimensional instantaneous nucleation, and three-dimensional diffusion controlled growth. Details can be found in reference [36]. We have applied this treatment to the -0.52 V current transient in Fig. 6 and have estimated that the charge associated with the two-dimensional growth process is approximately $85 \, \mu\text{C} \, \text{cm}^{-2}$. As stated previously, the Au electrode is covered with a partial upd layer at the starting potential of -0.40 V. Upon applying the -0.52 V deposition potential, the remainder of the complete Bi monolayer is formed. This is the equivalent of the 3rd voltammetric wave in Fig. 2. The charge under this peak is consistent with the $85 \, \mu\text{C} \, \text{cm}^{-2}$ charge obtained from the theoretical two-dimensional current transient. We therefore conclude that the small current peaks in the deposition current transients are associated with the completion of the Bi upd layer.

A non-dimensional plot of the current transient obtained at -0.52 V is shown in Fig. 7 together with the theoretical curves for instantaneous and progressive nucleation following the treatment of Scharifker and Hills [33]. The plot clearly suggests that Bi deposition onto Au proceeds by instantaneous nucleation. Using the equations derived in reference [33], i_{max} and t_{max} yielded a nucleation density of $3.96 \times 10^6 \, \text{cm}^{-2}$ for deposition at -0.52 V. The Bi upd contribution to the current transient is readily apparent in the non-dimensional plot. We have also examined the non-dimensional plot of the theoretical three-dimensional
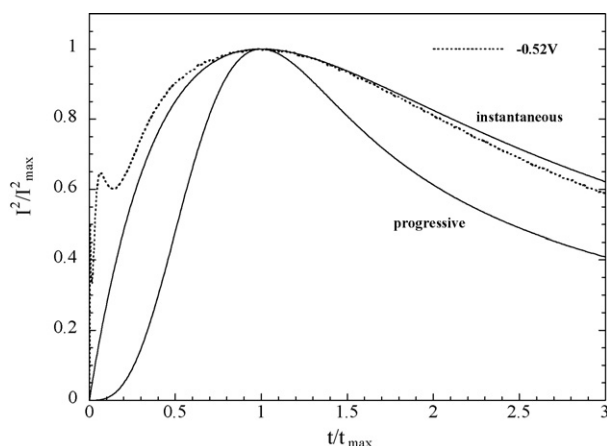
Fig. 7. Normalized −0.52 V current transient from Fig. 6 (- - - - -) compared to theoretical treatments (—) for three-dimensional instantaneous and progressive nucleation.

Fig. 9. Current density and resonant circuit resistance, R_1, during the same time period as Fig. 8.

current (from the Palomar-Pardave treatment) and see that it superimposes the theoretical curve for instantaneous nucleation.

The EQNB used in this study measures both the resonant frequency and the resistance R_1 of the equivalent resonant circuit, where shifts in the resonant frequency correspond to mass changes. The mass/charge ratio (m/Q) for the deposition or dissolution of Bi/Bi^{3+} assuming 100% current efficiency is $720\,\mu g\,C^{-1}$. Fig. 8 shows the values of the m/Q ratio during deposition and dissolution at various current densities up to $10\,mA\,cm^{-2}$ in $1.0\,mol\,L^{-1}$ HNO$_3$ containing $0.1\,mol\,L^{-1}$ Bi(NO$_3$)$_3$. The experimental values tend to be somewhat lower, about 80% of the theoretical. The lower efficiency is due to inhomogeneous deposition of Bi, which tends to accumulate at the rim of the electrode where the mass sensitivity of the EQNB is at a minimum [38,39]. The reduced sensitivity of the EQNB was confirmed by weighing the quartz crystal on an analytical balance before and after depositing about 3 mg of Bi. In spite of its lower precision, gravimetry gave an efficiency of 0.96 ± 0.04. This is a clear indication that the experimental m/Q ratio is depressed due to non-uniform current distribution.

While shifts in the resonant frequency correspond to mass changes, the value of R_1 is an indication of the mechanical losses
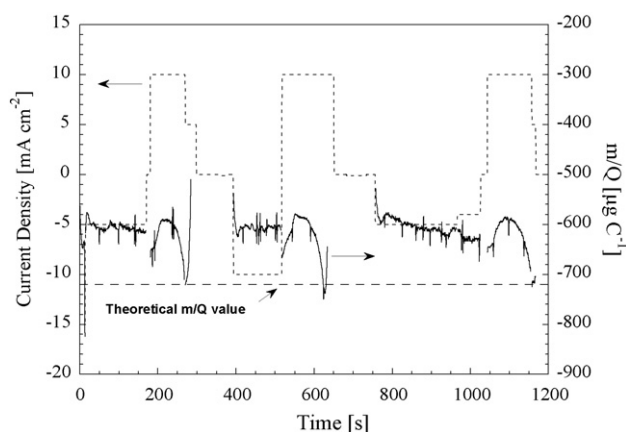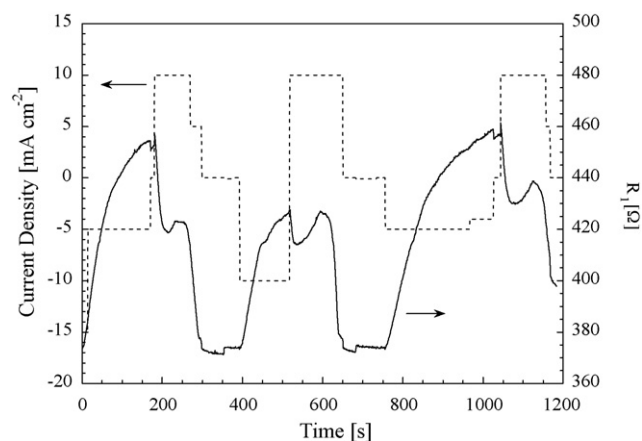

Fig. 8. The m/Q ratio during deposition and dissolution of Bi from $1.0\,mol\,L^{-1}$ HNO$_3$ containing $0.1\,mol\,L^{-1}$ Bi(NO$_3$)$_3$.

caused by entrainment of the solution in contact with the vibrating metal surface, and is therefore a sensitive indication of the roughness of the deposit [40]. Fig. 9 shows the changes in R_1 as measured during the same experiment and thus the same time frame as the data presented in Fig. 8. The initial values of R_1 of the originally smooth gold surface were close to $400\,\Omega$, while rough Bi deposits gave values up to $1\,k\Omega$. The roughening occurs very rapidly if the current density exceeds about $10\,mA\,cm^{-2}$. At current densities less than $10\,mA\,cm^{-2}$, R_1 increases rather sharply initially but tends to level off as the roughness reaches a steady state value. As the figure shows, R_1 decreases rapidly at the onset of the first anodic dissolution current. R_1 can be brought back to the original value by completely stripping the deposit from the Au surface.

Bismuth was electrodeposited onto planar substrates of evaporated Au and polycrystalline Cu using a variety of deposition potentials. All deposits were made from $1.0\,mol\,L^{-1}$ HNO$_3$ containing $0.10\,mol\,L^{-1}$ Bi(NO$_3$)$_3$. The coverage of the deposited films and surface morphology were characterized using FE-SEM. Fig. 10 shows the surfaces of 1.0 and $15\,\mu m$ films on both Au and Cu electrodeposited at -0.50 V. The $1.0\,\mu m$ films are nodular with grains measuring $1–2\,\mu m$. The $15\,\mu m$ films have the same nodular morphology as the $1.0\,\mu m$ thick films except that the average grain size is about a factor of four larger. Fig. 10 indicates that the surface morphology is identical for deposits formed on polycrystalline Cu and evaporated Au substrates under similar deposition conditions. The reversible potential for bismuth in $0.10\,mol\,L^{-1}$ Bi(NO$_3$)$_3$ solution is approximately -0.45 V versus SSE. Deposits made at a deposition potential of -0.50 V had a "frosty-white" appearance. The average deposition current at this potential was about $20\,mA\,cm^{-2}$. The visual appearance of the deposits became gradually darker due to roughening of the surface as more negative deposition potentials were applied.

In order to view a Bi film in cross-section, an electrodeposit was selectively ion milled using a FIB operating at 30 kV. Fig. 11 shows the cross-section of a nominal $15\,\mu m$ Bi film deposited galvanostatically at $5\,mA\,cm^{-2}$. The initial trench was made using 6600 pA and polishing of the cross-sectioned surface was

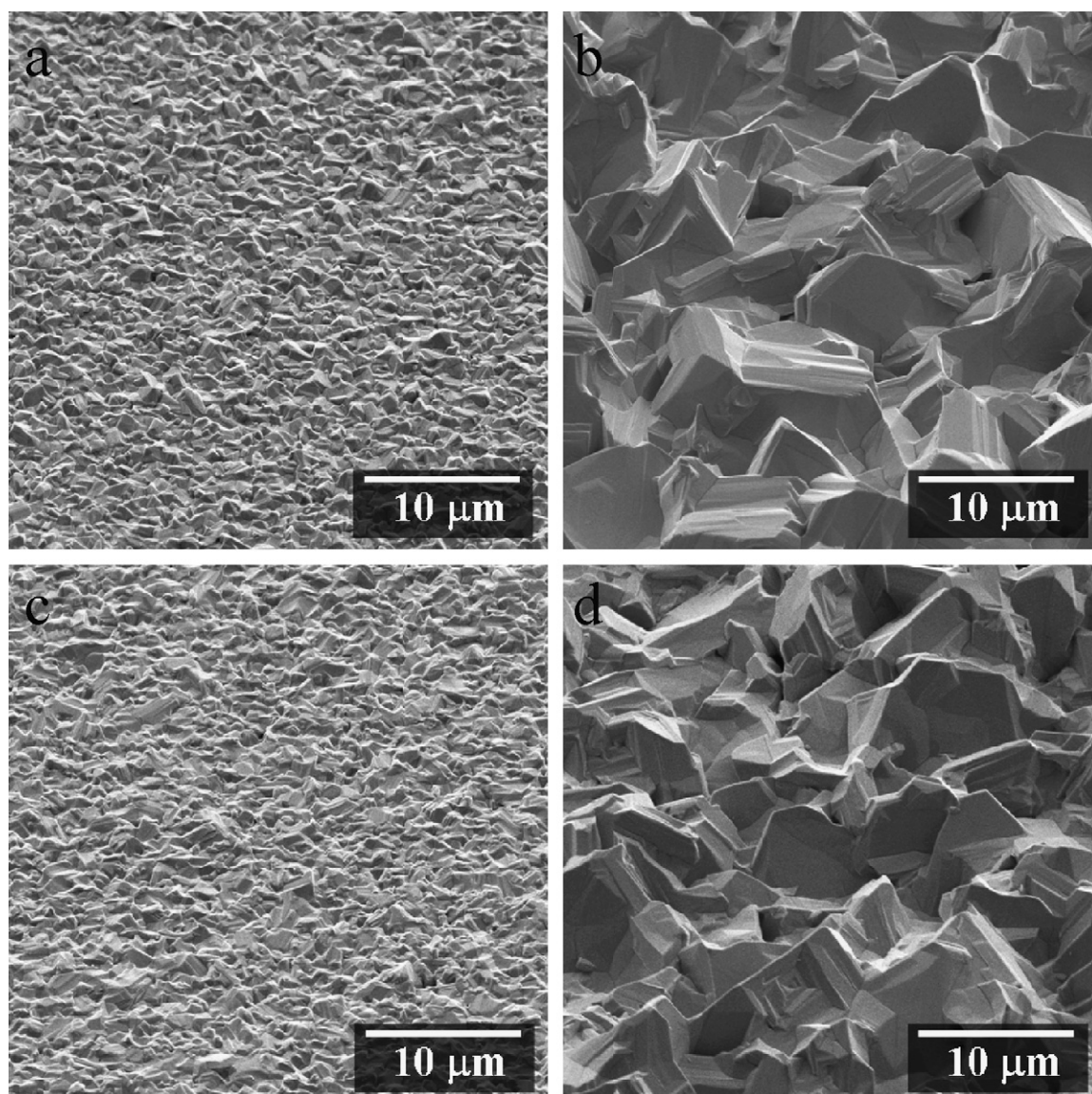Fig. 10. FE-SEM of as-deposited Bi surface following deposition at -0.50 V vs. SSE from $1.0\,mol\,L^{-1}$ HNO_3 containing $0.10\,mol\,L^{-1}$ $Bi(NO_3)_3$ (a) 1 µm thick Bi on evaporated Au, (b) 15 µm thick Bi on evaporated Au, (c) 1 µm thick Bi on polycrystalline Cu, and (d) 15 µm thick Bi on polycrystalline Cu.
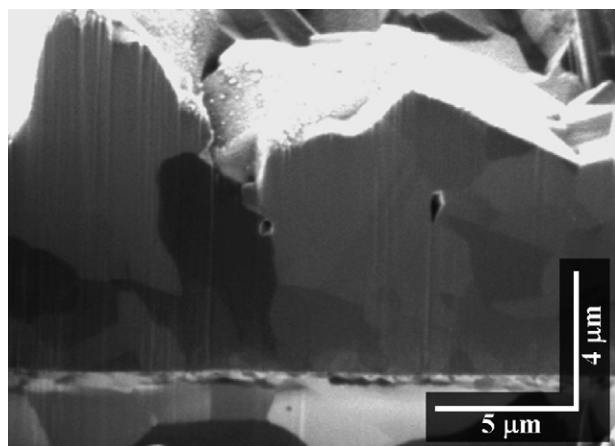

Fig. 11. FE-SEM of a FIBed cross-section of a nominal 15 µm thick Bi deposit made at constant current density of $5\,mA\,cm^{-2}$.

completed with 350 pA. The FE-SEM image reveals that the size of the grains varies between 1 and 5 µm. The copper substrate is visible beneath the Bi layer. There is no visible reaction at the Cu–Bi interface as expected since Cu and Bi have negligible mutual solubility and no intermetallic compounds form in this system [41]. Small voids are occasionally observed at the Bi grain boundaries. This is likely due to the nodular growth of the electrodeposit where intergranular regions fail to fill completely.

Fig. 12 shows powder X-ray diffraction patterns of 1.0 µm thick bismuth films electrodeposited onto evaporated Au substrates at various overpotentials. The positions of reflections due to the gold substrate are designated by triangles at the top of the figure; however only the 1 1 1 is visible due to the strong crystallographic texture of the evaporated Au film. Bismuth has a rhombohedral crystal structure (space group $R-3m$); however, a hexagonal primitive cell is usually used to describe the bismuth lattice. In this paper we use the three-index Miller system of
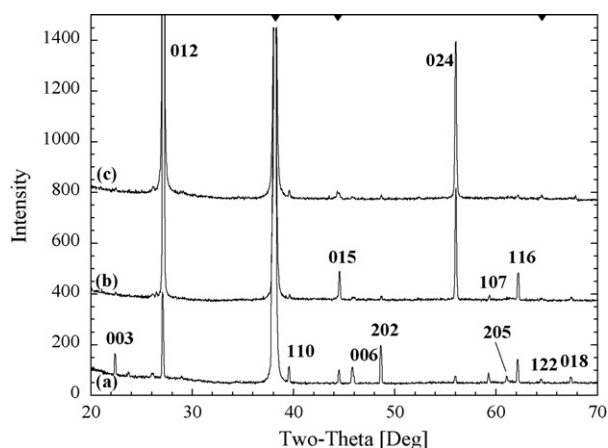
Fig. 12. XRD patterns (Cu Kα) of 1.0 μm bismuth films electrodeposited onto evaporated Au substrates at 25 °C from 1.0 mol L^{-1} HNO$_3$ containing 0.10 mol L^{-1} Bi(NO$_3$)$_3$ (a) −0.50 V, (b) −0.55 V, and (c) −0.65 V. The triangles at the top of the figure represent the reflections due to the gold substrate.

Fig. 13. Texture profiles (0 2 4) for 1.0 μm thick bismuth films electrodeposited at 25 °C from 1.0 mol L^{-1} HNO$_3$ containing 0.10 mol L^{-1} Bi(NO$_3$)$_3$ onto evaporated Au at (a) −0.50 V, (b) −0.55 V, and (c) −0.65 V; and polycrystalline Cu at (d) −0.50 V, (e) −0.55 V, and (f) −0.65 V.

Table 1
The FWHM of the 024 texture profiles shown in Fig. 13 for 1.0 μm thick bismuth films electrodeposited onto evaporated Au and polycrystalline Cu substrates

Substrate	Potential	FWHM
Au	−0.50	180.0
Au	−0.55	18.3
Au	−0.65	11.2
Cu	−0.50	40.0
Cu	−0.55	28.5
Cu	−0.65	23.9

indices rather than the four-index Miller-Bravais system [42]; the third of the four indices is omitted. All of the diffraction patterns can be indexed to bismuth with lattice parameters $a = 0.455$ nm and $c = 1.186$ nm. It is readily apparent from Fig. 12 that the texture of the Bi electrodeposit changes with overpotential. As the deposition potential is made more negative, the intensity of the 0 1 2 and 0 2 4 reflections increases significantly while the intensity of several other reflections, such as the 0 0 3, 1 1 0 and 2 0 2, decrease, suggesting preferred orientation of (0 1 2) planes parallel to the film.

The texture of the films was further investigated with a technique developed for analyzing fiber texture using a powder diffractometer [43,44]. The Bragg peak of the textured planes was scanned and the detector was then set at the position of the peak center ($2\theta_B$). The diffracted intensity was measured as the sample was rotated over as large an angular range as possible, from glancing incidence to incidence at close to $2\theta_B$, and corrections were applied to the intensity profile to allow for defocusing and absorption, yielding a corrected rocking curve. The Bragg peaks selected for texture analysis were the most intense in Fig. 12, the 0 1 2 and the 0 2 4, which both measure texture on (0 1 2) planes. The 0 1 2 peak is more intense, but the 0 2 4, with its larger Bragg angle allows texture to be measured over a larger angular range. The 0 2 4 rocking curves for the Bi-on-Au and Bi-on-Cu films deposited at various overpotentials, normalized to a maximum value of 1.0 in all cases, are given in Fig. 13. The curves show that the level of texture (as indicated by the sharpness of the rocking curve profile) increased as the overpotential increased. For each profile the full width at half maximum intensity (FWHM) was measured and the results are given in Table 1. In the case of Bi-on-Au deposited at −0.50 V, there was no peak in the texture profile, indicating no preferred orientation of the (0 1 2) planes and so the FWHM could not be measured. Table 1 clearly shows that FWHM of the 0 2 4 rocking curve decreases with increasing overpotential and that the texture of the Bi-on-Au films at the higher overpotentials was greater than for the Bi-on-Cu deposits.
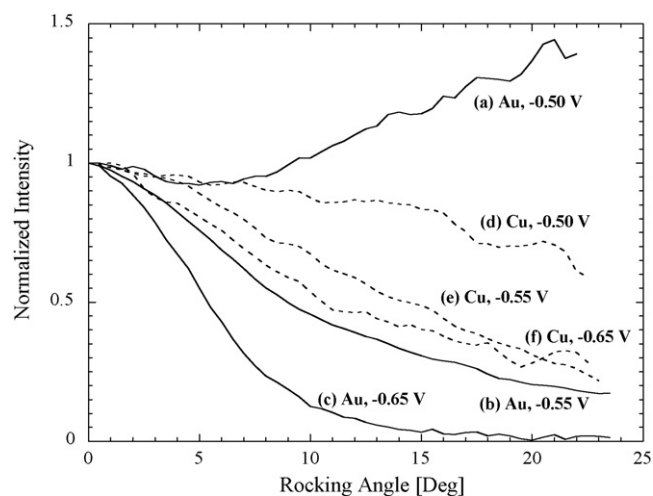
Bismuth films with preferred (0 1 2) orientation have been reported in the literature. Vereecken has shown that polycrystalline Bi films electrodeposited onto p-GaAs (1 0 0) form large grains with preferred 0 1 2 orientation after annealing at temperatures just below the melting point [10], suggesting that (0 1 2) is a low energy plane. The fact that the preferred (0 1 2) orientation occurs at higher overpotential is somewhat surprising since films grown at higher deposition rates typically have a more random structure. The stronger preferred (0 1 2) orientation on (1 1 1)-textured Au than polycrystalline Cu may be attributed to the Bi upd layer that forms on Au (1 1 1). The fully formed ($p \times \sqrt{3}$)-2Bi adlayer consists of a rectangular array of atoms measuring 0.447 nm by 0.49 nm [16,23,29–31]. Similarly, the (0 1 2) plane of Bi consists of a rectangular lattice of atoms, 0.455 nm by 0.475 nm. This matches well with the spacing of the ($p \times \sqrt{3}$)-2Bi adlayer. The mismatch in the first dimension is +1.8% and in the second it is −3.1%. Although the bulk deposition of Bi onto Au proceeds by three-dimensional nucleation and growth, these islands are formed on the ($p \times \sqrt{3}$)-2Bi adlayer which influences the crystallographic orientation of the Bi nuclei.

4. Conclusions

The electrodeposition of bismuth on a number of metallic substrates from nitrate solutions can be performed successfully,

obtaining compact, although rather rough, deposits, with 100% current efficiency. The deposits appear to begin by instantaneous nucleation over the whole substrate surface, and have a grain size varying from 1 to 5 μm. The texture of the Bi deposits on Cu and Au was investigated in detail as a function of the deposition voltage. It was found that at more negative potential, that is at higher current density, there is a pronounced tendency to develop a (0 1 2) texture, particularly on the (1 1 1)-textured Au substrate. A preferred (0 1 2) texture on Au is not surprising since three-dimensional growth is preceded by a $(p \times \sqrt{3})$-2Bi upd layer which has identical in-plane symmetry and very similar lattice spacings to the (0 1 2) plane of Bi.

References

[1] S. Cho, Y. Kim, L.J. Olafsen, I. Vurgaftman, A.J. Freeman, G.K.L. Wong, J.R. Meyer, C.A. Hoffmann, J.B. Ketterson, J. Magn. Magn. Mater. 239 (2002) 201.
[2] S. Jiang, Y.H. Huang, F. Luo, N. Du, C.H. Yan, Inorg. Chem. Commun. 6 (2003) 781.
[3] R.A. Tolutis, S. Balevicius, Phys. Status Solidi A 203 (2006) 600.
[4] L. Li, Y. Zhang, G. Li, L. Zhang, Chem. Phys. Lett. 378 (2003) 244.
[5] M. Lu, R.J. Zieve, A. van Hulst, H.M. Jaeger, T.F. Rosenbaum, S. Radelaar, Phys. Rev. B 53 (1996) 1609.
[6] J.P. Ziegler, Solar Energy Mater. 56 (1999) 477.
[7] S.I.C. deTorresi, I.A. Carlos, J. Electroanal. Chem. 414 (1996) 11.
[8] A.J. Bard (Ed.), Encyclopedia of Electrochemistry of the Elements, vol. IX, Part B, Marcel Dekker, Inc., New York, USA, 1986.
[9] P.M. Vereecken, K. Rodbell, C.X. Ji, P.C. Searson, Appl. Phys. Lett. 86 (2005) 121916.
[10] P.M. Vereecken, L. Sun, P.C. Searson, M. Tanase, D.H. Reich, C.L. Chien, J. Appl. Phys. 88 (2000) 6529.
[11] P.M. Vereecken, P.C. Searson, J. Electrochem. Soc. 148 (2001) C733.
[12] J. Wang, Electroanalysis 17 (2005) 1341.
[13] A. Krolicka, A. Bobrowski, Electrochem. Commun. 6 (2004) 99.
[14] I. Svancara, K. Vytras, Chem. Listy 100 (2006) 90.
[15] S. Sayed, K. Jüttner, Electrochim. Acta 28 (1983) 1635.
[16] C.-H. Chen, A. Gewirth, J. Am. Chem. Soc. 114 (1992) 5439.
[17] S. Campbell, R. Parsons, J. Chem. Soc. Faraday Trans. 88 (1992) 833.
[18] S. Chang, Y. Ho, M. Weaver, Surf. Sci. (1992) 81.
[19] J. Clavilier, A. Fernandez-Vega, J.M. Feliu, A. Aldaz, J. Electroanal. Chem. 258 (1989) 89.
[20] E. Herrero, A. Fernandez-Vega, J.M. Feliu, A. Aldaz, J. Electroanal. Chem. 350 (1993) 73.
[21] S.P.E. Smith, H.A. Abruna, J. Phys. Chem. B 102 (1998) 3506.
[22] M. Yang, Z. Hu, J. Electroanal. Chem. 583 (2005) 46.
[23] C.A. Jeffrey, D.A. Harrington, S. Morin, Surf. Sci. 512 (2002) L367.
[24] R. Piontelli, G. Poli, Gazz. Chim. Ital. 79 (1949) 981.
[25] R.C. Weast (Ed.), Handbook of Chemistry and Physics, 66 ed., CRC Press, Inc., Boca Raton, Florida, 1985–1986.
[26] G.E. Dima, A.C.A. de Vooys, M.T.M. Koper, J. Electroanal. Chem. 554–555 (2003) 15.
[27] T. Solomun, W. Kautek, Electrochim. Acta 47 (2001) 679.
[28] G.R. Stafford, U. Bertocci, J. Phys. Chem. B (2006) 15493.
[29] C.-H. Chen, K.D. Kepler, A.A. Gewirth, B.M. Ocko, J. Wang, J. Phys. Chem. 97 (1993) 7290.
[30] B.K. Niece, A.A. Gewirth, Langmuir 12 (1996) 4909.
[31] K. Tamura, J. Wang, R. Adzic, B. Ocko, J. Phys. Chem. B 108 (2004) 1992.
[32] T. Berzins, P. Delahay, J. Am. Chem. Soc. 75 (1953) 555.
[33] B. Scharifker, G. Hills, Electrochim. Acta 28 (1983) 879.
[34] L.H. Mendoza-Huizar, J. Robles, M. Palomar-Pardave, J. Electroanal. Chem. 545 (2003) 39.
[35] L.H. Mendoza-Huizar, J. Robles, M. Palomar-Pardave, J. Electrochem. Soc. 152 (2005) C265.
[36] M. Palomar-Pardave, I. Gonzalez, N. Batina, J. Phys. Chem. B 2000 (2000) 3545.
[37] M. Palomar-Pardave, M. Miranda-Hernandez, I. Gonzalez, N. Batina, Surf. Sci. 399 (1998) 80.
[38] M.D. Ward, E.J. Delawski, Anal. Chem. 63 (1991) 886.
[39] A.C. Hillier, M.D. Ward, Anal. Chem. 64 (1992) 2539.
[40] M. Wünsche, H. Meyer, R. Schumacher, S. Wasle, K. Doblhofer, Z. Physik. Chem. 208 (1999) 225.
[41] T.B. Massalski (Ed.), Binary Alloy Phase Diagrams, American Society for Metals, Metals Park, OH, 1986.
[42] F.C. Frank, Acta Cryst. 18 (1965) 862.
[43] M.D. Vaudin, TexturePlus, National Institute of Standards and Technology, Ceramics Division, Gaithersburg, MD (program available by written request (E-mail: mark.vaudin@nist.gov) or on the World Wide Web at http://www.ceramics.nist.gov/webbook/TexturePlus/texture.htm).
[44] M.D. Vaudin, M.W. Rupich, M. Jowett, G.N. Riley, J.F. Bingert, J. Mater. Res. 13 (1998) 2910.